Artery-Vein Separation of Human Vasculature from 3D Thoracic CT Angio Scans

Sangmin Park & Chandrajit Bajaj
Computational Visualization Center,
Department of Computer Sciences,
Institute of Computational Engineering and Sciences,
University of Texas at Austin,
Austin, Texas 78712

Gregory Gladish, MD
Diagnostic Radiology,
The University of Texas M.D. Anderson Cancer Center,
Houston, Texas 77030

ABSTRACT: This paper presents vascular tree reconstruction and artery-vein separation methods from 3D thoracic CT-angiography (CTA) images. In the methods, the lungs, blood vessels and the heart are segmented by using intensity-based thresholds and morphological operations. After the distance transform for the regions of blood vessels and the heart, we compute seed points that are the maxima of distance values. At each seed point, spheres are inflated until hit a boundary. The spheres and the connections between overlapped spheres make a graph representation of the 3D image. Once the pulmonary trunk is detected by using directions in the graph, blood vessels are traversed toward the heart, while merging and verifying branches. If a branch is linked to the pulmonary trunk, then all subsegmental trees of the branch are classified into pulmonary arteries. Otherwise, it is a pulmonary vein.

1 INTRODUCTION

Human vasculature reconstruction from three-dimensional (3D) computed tomography (CT) images of the thorax is a critical step for computer-aided diagnosis (CAD) in disease domains such as lung nodules (Gady Agam 2005), coronary artery disease (Jamshid Dehmeshki and Qanadli 2004), and pulmonary embolism (PE) (Yoshitaka Masutani 2002). It remains a challenging problem even though there have been many published approaches (Kirbas and Quek 2004) (Katja Bühler and Cruz 2003).

Thoracic CT angiography (CTA) imaging is often performed for patients suspected of having pulmonary embolus (PE) that is defined as a thrombus (or a clot of blood) (Schoepf and Costello 2004). However, blood vessel extraction is often not enough for PE detection from CTA, since the position of thrombi is always in the pulmonary trunk and/or the subsegmental arteries (Hartmann and Prokop 2002). Differentiation of pulmonary arterial from venous trees significantly reduces false positive PE detection in pulmonary veins. While several authors have addressed the issue of artery-vein separation (AV separation) from magnetic-resonance angiography (MRA) (Cornelis M. van Bemmel and Niessen 2003) (Stefancik and Sonka 2001) (Tianhu Lei and Odhner 2001) (Michael Bock 2000), Sluimer *et al.* mentions that AV separation from CTA is one of their primary future challenges (Ingrid Sluimer and van Ginneken 2006).

For AV separation from MRA, Bemmel *et al.* suggests a level-set framework (Cornelis M. van Bemmel and Niessen 2003). In their method, the central arterial and venous axes are determined by using a supervised learning (SL) procedure. Their SL method computes a minimum-cost path between two (or more) user-defined points in the arterial and venous parts of the vasculature. The high probability voxels which become part of the center of a vascular structure are enhanced using a multiscale filter. Stefancik and Sonka show that a graph search algorithm coupled to a knowledge-based approach could be applied to AV separation (Stefancik and Sonka 2001). Lei *et al.* utilized the principles and algorithms of fuzzy connected object delineation, for AV separation (Tianhu Lei and Odhner 2001). Bock *et al.* proposed correlation analysis between manually selected regions of interest and the acquired 3D MRA data sets, viewed as a time series (Michael Bock 2000). Since diverse medical imaging modalities require different approaches (Kirbas and Quek 2004), in this paper we focus on robust AV separation approach from 3D thoracic CTA images, knowing that the features of CTA images are quite different from MRA.

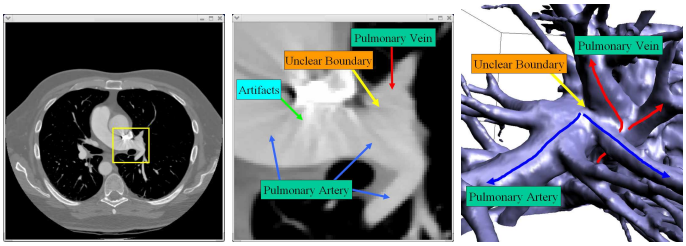

(a) CTA slice (b) Enlarged image (c) Iso-surfaces

Figure 1: Slice images of CT-angiography and Iso-surfaces: The yellow box of (a) is enlarged in (b) that shows the unclear boundary between the pulmonary artery and vein and the same region is visualized in (c) with iso-surfaces.

Fig. 1 (a,b) (image slices) and (c) (3D iso-surface) show some of the main problems that make it difficult to differentiate pulmonary arterial and venous trees from 3D thoracic CTA images. First, since the resolution of CTA images is limited and the artery and vein are very close to each other, there is an unclear boundary between them. The same problem is present in many other places even in a single data set. Fig. 2 shows another region that contains the similar problem. Second, the bright area in Fig. 1(b), which represents the vena cava, ~~possesses~~ many neighboring CTA artifacts. Since the artifacts are more distinct than the unclear boundary in Fig. 1(b), they are difficult to remove as unnecessary features, while identifying the unclear boundaries.

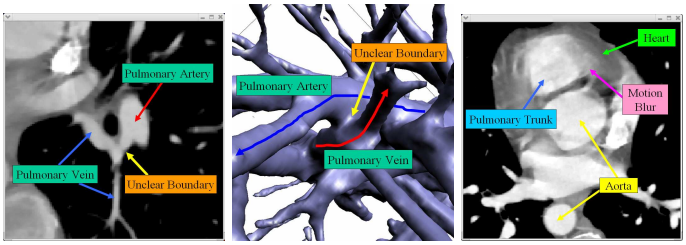

(a) CTA slice (b) Iso-surface (c) Motion Blur

Figure 2: There are many unclear boundaries in 3D CTA images. It makes it hard to separate pulmonary arteries and veins.

The unclear boundary problem is addressed by Bemmel *et al.* in (Cornelis M. van Bemmel and Niessen 2003). In their method, voxels are labeled arterial or venous based on the arrival time of the respective level-set fronts. The front evolution is depend on three external forces based on the information of intensity, gradient, and vesselness. However, the labeling approach does not work properly for the problem region of Fig. 1(b), since the pulmonary artery is thicker than the vein, and the evolution of level-set fronts can be hampered by high gradients at the artifacts. Furthermore, since there are many unclear boundaries between pulmonary arteries and veins in 3D thoracic CTA images, all the problem regions should be skeletonized before using the level-set framework, which requires heavy user interactions. Kiraly *et al.* used branching angles to remove false branches for only arterial subtrees distal to a site of PE (Atilla P. Kiraly and Novak 2004). Finally, Bülow *et al.* proposed an algorithm for pulmonary arterial tree extraction. It is based on the fact that pulmonary arteries accompany the bronchial tree (Tomas Bülow 2005). The mislabeling of the algorithm increases as vessel radius decreases and it is not specifically evaluated.

Fig. 2(c) shows another problem in 3D CTA images. Since the heart keeps beating, when the images are taken, it causes motion blur and the heart boundaries are ambiguous. In this paper, we suggest AV separation methods that solve the problems of distinct artifacts, unclear boundaries between arteries and veins, motion blur effects.

This ~~papers~~ organized as follows. In Section 2, we present algorithms for the segmentation of lungs, blood vessels and the heart and address the pulmonary trunk detection from a graph. In Section 3, we describe the blood vessel tracking and AV separation methods. Finally, in Section 4, we show the results and evaluation of the AV separation and indicate the direction of future work.

2 PULMONARY TRUNK DETECTION

For AV separation, we use the fact that all pulmonary arteries are connected to the pulmonary trunk that is one of the main branches of the heart. The trunk comes out from the right ventricle of the heart and diverges to the left and right lungs. If there is a path from a branch to the pulmonary trunk within blood vessels, then we can say that the branch is a part of the pulmonary arterial trees. Once pulmonary arteries are extracted, it is assumed that all other blood vessels, which are linked with other parts of the heart, are pulmonary veins. Our AV separation method is composed of 5 steps.

First, we use multilevel thresholds to extract lungs and blood vessels. Automatic lung extraction has been addressed in several papers such as (Shiying Hu and Reinhardt 2001), (Binsheng Zhao and Schwartz 2003), and (Armato III and Sensakovi 2004). Our lung extraction method is similar to those algorithms in terms of using multilevel thresholds and component analysis, but we do not consider left-right lung distinction and the trachea and bronchi segmentation, since the segmented lungs are used to remove unnecessary bones that are the outside of the lungs and have similar intensity ranges to blood vessels. Fig. 3 shows the results of the lung extraction and the thresholding for blood vessels.

Second, to reduce the search space, the bones are removed by using smooth surfaces, which are defined by grid points. Each grid point moves along grid lines that are orthogonal to each initial surface. At the be-

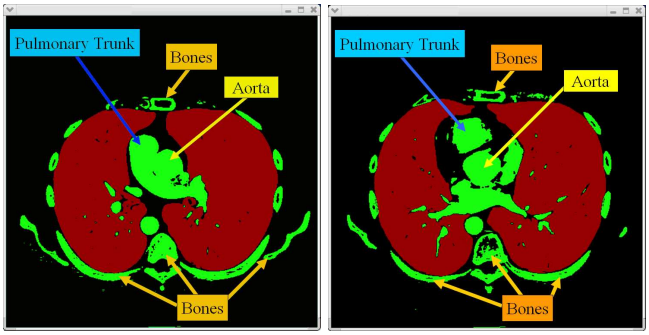

(a) Slice No. 163 (b) Slice No. 201

Figure 3: Binary classification of lungs and blood vessels: Brown color represents the two lungs, while green color corresponds to many different objects such as arteries, veins, heart, and bones.

ginning, four flat surfaces are located at the left, right, top and bottom data boundary and move toward the center of the data, until hit the extracted lungs (Brown color in Fig. 4). Each grid point location at $L(i,j)$ is adjusted by the smoothing convolution (Eq. 1) with the restriction that each surface patch composed by four grid points cannot penetrate the lungs. Once the locations of each grid point are computed, all voxels behind the surfaces are set to zero. The smoothing convolution is computed by

$$O(i,j) = \sum_{k=-m}^{m} \sum_{l=-n}^{n} L(i+k, j+l) \times K(k+m, l+n), \quad (1)$$

where $K()$ represents the kernel with the size of $(2m+1) \times (2n+1)$: The 5×5 and 7×7 kernels are used for the surfaces in Fig. 4(a) and Fig. 4(b) respectively.

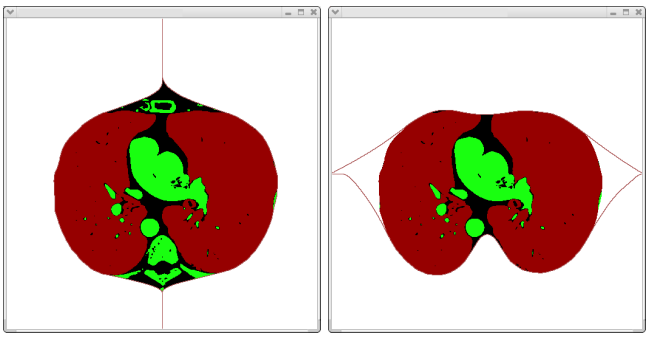

(a) (b)

Figure 4: (a) Horizontally moving surfaces, (b) Vertically moving surfaces: To reduce the search space, bones are removed by using smooth surfaces. The planes start at left, right, top and bottom locations and move toward the center of the image until hit the lungs. After each surface is smoothed by a convolution, all voxels behind the surfaces are set to zero.

Third, for the pulmonary trunk detection, we separate the heart area using dilation, which is one of the morphological operations (Chen and Haralick 1995). We extend the dilation definition to 3D image space (Z^3) with foreground, $F \in Z^3$, and a structuring element, $S_r \in Z^3$, as following, $F \oplus S_r = \{c \in Z^3 \mid c = a + b \text{ for some } a \in F \text{ and } b \in S\}$, where r represents the radius of the sphere structuring element. In other words, after the dilation operation, a background voxel is set to foreground value, only when at least one voxel in the structuring element coincides with a foreground voxel.

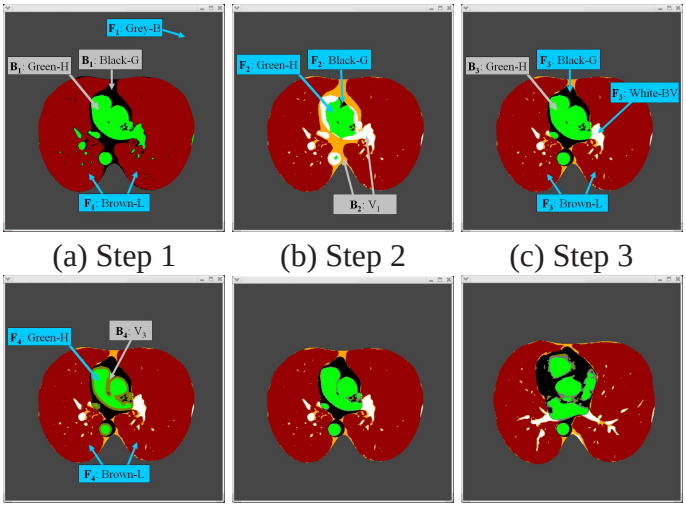

(a) Step 1 (b) Step 2 (c) Step 3

(d) Step 4 (e) Final Results (#163 and #201)

Figure 5: Morphological Operations: In this operations, the heart area and blood vessels are separated and the unclear boundaries caused by the motion blur effects are redefined.

In the first step of our morphological operations, two lungs (Brown-L) and the background voxels (Grey-B), which are set to zero in the bone removing step, work as the foreground (F_1) and the heart and blood vessels (Green-H) and ~~gabs~~ (Black-G) are the background (B_1) (See Fig. 5(a)). Unlike general dilation, the background colors are replaced with new colors that are not used in the image. The new color voxels work as new groups in the following steps. Fig. 5(b) shows the new group voxels (V_1) computed by the first dilation step. V_1 is used as the background (B_2) and ~~Grren~~ H and Black-G are the foreground (F_2) in the second step. After the second step, the heart area (green) and small blood vessels (white) are separated (See Fig. 5(c)). The third and forth steps are to remove the motion blur effects caused by the beating heart and redefine the heart boundaries. The new boundary may be different from the real heart boundary, but it is good enough for pulmonary trunk detection. The entire sequence of steps is as follows:

F_1 =Brown-L $\cup$ Grey-B, B_1=Green-H $\cup$ Black-G, V_1=$(F_1 \oplus S_{16}) \cap B_1$,
F_2 =Green-H $\cup$ Black-G, B_2= V_1, V_2= $F_2 \oplus S_{16}$,
F_3 =White-BV $\cup$ Black-G $\cup$ Brown-L, B_3=Green-H, V_3=$F_3 \oplus S_5$, and
F_4 =Green-H $\cup$ Brown-L, B_4=V_3, V_4=$F_4 \oplus S_4$.

Fourth, after the morphological operations, we apply the distance transform (Saito and Toriwaki 1994) to the green (the heart and its main branches) and white (blood vessels) regions in Fig. 5(e) to compute seed points that are local maxima of the distance values (See Fig. 6). At each seed point location, a sphere denoted by S_{id} is generated. Each sphere S_{id} is represented by the center C_{id} and the radius R_{id}. To compute R_{id}, spheres are inflated at C_{id} until any part of the sphere surface hits a boundary that is defined as the surface of the green area in Fig. 5(e). To reduce the number of spheres, some spheres with centers that are covered by a larger sphere are removed. When two spheres are overlapped, the spheres have a connection between them. All overlapped spheres with S_a are the neighbors of S_a. Let N_a be the neighbor set of S_a.

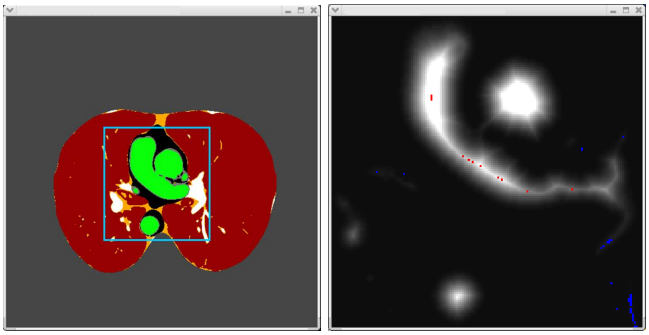

(a) Slice No. 158 (b) Distance Map

Figure 6: Distance Transform: (b) shows the distance map of the left box of (a). The red voxels represent the local maxima of the distance values in the green region of (a). The blue local maxima are in the white area of (a).

Some initial spheres generated by the above method ~~can be separated~~ from the main group that has the biggest number of connected spheres. To connect those spheres to the main group, the following two rules are applied, until all spheres have more than one neighbor.

Rule 1 If there exists a sphere, S_a, such that $|N_a| = 1$, then a new sphere, S_c, is generated. Let $N_a = \{S_b\}$ and $N_c = \emptyset$. To compute C_n and R_n, we define the set M_1 of voxel locations that satisfy the following conditions $R_a < D_{ao} \leq R_a + 2$ and $V_{ao} \cdot V_{ba} > 0$, where D_{ao} is the Euclidean distance between C_a and a voxel location L_o and V_{ao} is the normalized vector from C_a to L_o. C_n is one of the elements of M_1 that maximizes R_c. If there are more than two voxel locations that have the same maximum radius, then we pick a voxel location that has the maximum value of $V_{ao} \cdot V_{ba}$. Once S_c is added, the neighbor sets of N_a and N_c change to $\{S_b,\ S_c\}$ and $\{S_a\}$ respectively.

Rule 2 If there exists an isolated sphere, S_d such that $|N_d| = 0$, then a new sphere, S_e, is generated at $C_d \in M_2$ that maximizes R_d, where M_2 is a set of voxel locations that have the distance between R_d and $R_d + 1$ from C_d.

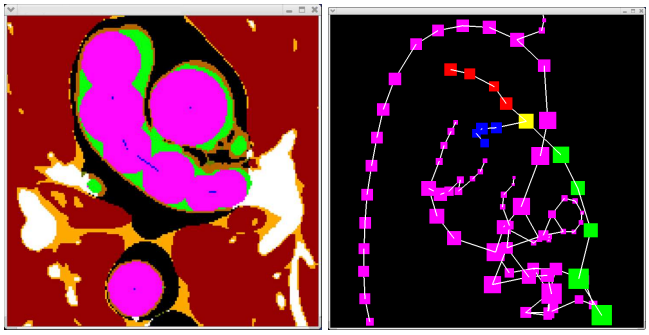

(a) Slice No. 158 (b) Graph Representation

Figure 7: Spheres and Medial Axis: The purple spheres are generated in the green heart area. The blue lines connecting the overlapped spheres are skeletons in (a). The graph representation of (b) shows the pulmonary trunk (green) and two branches that go to the left(red boxes) and right (blue boxes) lungs. The graph contains not only skeletons, but also blood vessel thickness at the sampled box locations

Finally, after all the above steps, the 3D CTA image space (Fig. 7(a)) changes to a graph representation (Fig. 7(b)). To detect the pulmonary trunk in the graph, we use direction vectors in the 3D space defined by three orthogonal axes X (horizontal), Y (vertical), and Z (perpendicular to slices). The origin is located at the top left corner of the first slice. The X and Y axes increase as go right and down in image slices respectively and the Z axis increases as the slice number increases. We search the sphere S_{ctr} (The yellow box in Fig. 7(b)) that has three branches and their direction vectors are (X_1, Y_1, Z_1), (X_2, Y_2, Z_2) and (X_3, Y_3, Z_3) that have 3-5 spheres per each branch and satisfy the following properties:

$$(\|Z_1\| > \|X_1\| \text{ or } \|Z_1\| > \|Y_1\|),\ Y_1 < 0,\ Z_1 > 0,$$
$$(\|X_2\| > \|Z_2\| \text{ or } \|Y_2\| > \|Z_2\|),\ X_2 < 0,\ Y_2 > 0,$$
$$\text{and}$$
$$(\|X_3\| > \|Z_3\| \text{ or } \|Y_3\| > \|Z_3\|),\ X_3 > 0,\ Y_3 > 0.$$

The green, red and blue boxes in Fig. 7(b) follow the above three criteria respectively. Once the pulmonary trunk and two branches are detected, all connections between the three branches are all other spheres are removed to separate the pulmonary arteries from veins.

3 BLOOD VESSEL EXTRACTION

To solve the ambiguous boundary problem (depicted in Fig. 1 and 2), we suggest a new vascular tree reconstruction algorithm as follows: First, spheres are generated at each blue seed point of Fig. 6(b) by using

the same methods explained in the previous section (The fourth step) such as inflation, small radius sphere removals and neighbor connections. Second, we find all possible dead ends of blood vessels. In fact, blood vessels do not have dead ends in the human body, but as they branch and become more distant from the heart, the vascular diameter decreases and blood vessels disappear in 3D CTA images. Therefore, there are many blood vessel dead ends in the image data. Third, at each dead end, spheres are added toward the opposite directions of the dead ends by Rule 1 defined in the previous section. When two spheres, S_2 and S_4 are overlapped (Fig. 8(a) and 9(a)), spheres are pre-generated along the blood vessel directions, V_{12} and V_{34}, (Fig. 8(b) and 9(b)) to verify the merging. If the lines between the pre-generated sphere centers are totally in the inside of blood vessels, then the two spheres, S_2 and S_4, should be merged and connected to S_5 (Fig. 8(c)). Otherwise, there exist two different branches along the two different directions (See Fig. 9(c)). Finally, each sphere, which is close to the heart, is connected to one of the heart spheres in Fig. 7 based on branch directions.

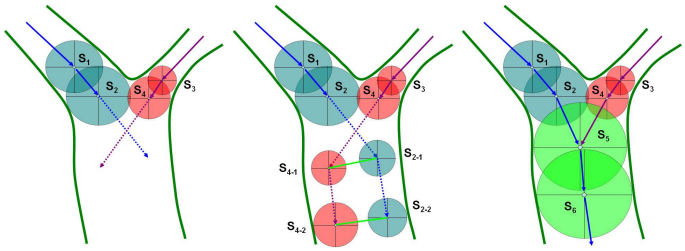

(a) Connection (b) Pre-generation (c) Solution

Figure 8: Branch Merging: To verify the connection between S_2 and S_4, spheres are pre-generated along the directions of V_{12} and V_{34}. If the lines connecting the sphere centers (C_{2-1}, C_{4-1}) and (C_{2-2}, C_{4-2}) are totally in the inside of blood vessel, then S_5 is generated and S_2 and S_4 are the neighbors of S_5.

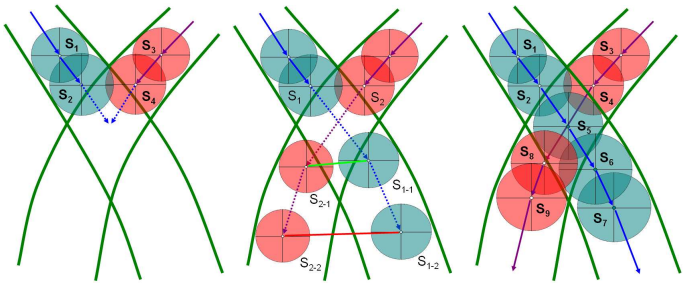

(a) Connection (b) Pre-generation (c) Solution

Figure 9: Branch Separation: If at least one line between the pre-generated sphere centers is in the outside of blood vessels (the red line in (b) between S_{2-2} and S_{4-2}), then there exist two different branches along V_{12} and V_{34}.

The above algorithm can solve the unclear boundary problem of Fig. 2, but Fig. 1, since the branch separation test of Fig. 9 ~~is failed~~ in the heart area. Therefore, we suggest a knowledge-based searching method for the problem of Fig. 1. In the method, we compute initial skeletons by connecting the local maxima of Fig. 6 along the ridges of the distance map, which is similar to Bitter *et al*'s algorithm (Ingmar Bitter and Sato 2001).

At the end sphere of the right pulmonary artery branch in Fig. 7(a), the direction of the thickest artery branch (X_r, Y_r, Z_r) has the following properties: $\|X_r\| > 0$, $\|Y_r\| > 0$ and $\|Z_r\| > 0$, while the direction of the pulmonary vein (X_v, Y_v, Z_v) has the feature of $\|X_v\| < 0$, $\|Y_v\| > 0$ and $\|Z_v\| > 0$ (See Fig. 1(c)). Since the boundary between the pulmonary artery and vein is not clear, there exist a wrong skeleton that passes through the boundary. After searching the pulmonary artery and vein via the knowledge-based method, we can remove the wrong skeletons and re-define a rough boundary between them.

4 RESULTS

After all the above steps, all spheres that are connected to the pulmonary trunk are pulmonary artery. All others that have links to any part of the heart are pulmonary vein. Fig. 10(a) shows the spheres and skeletons. The blue color boxes represent pulmonary arteries that are connected to the pulmonary trunk. Fig. 10(b,c) contains the results of our AV separation algorithm. Fig. 10(b) is the same region as Fig. 1(c) and Fig. 10(c) shows the area of Fig. 2(b).

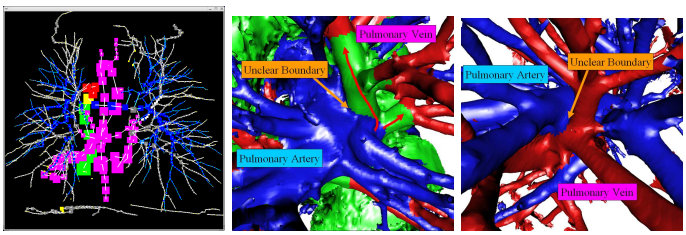

(a) Skeletons (b) Region 1 (c) Region 2

Figure 10: AV Separation Results

To verify our AV separation methods, we applied the methods to 6 datasets and counted wrong labeling and missing branches. The average number of incorrect labels is around 5 and the average number of missing branches is around 6. Our methods need to be evaluated on larger data sets. Automatic pulmonary embolus detection is the future work of this research.

5 ACKNOWLEDGMENTS

First and second authors are supported in part by NSF grants ITR-EIA-0325550, CNS-0540033 and NIH grants P20 RR020647, R01 GM074258-021 and R01-GM073087.

REFERENCES

Armato III, S. G. and W. F. Sensakovi (2004). Automated lung segmentation for thoracic ct: Impact on computer-aided diagnosis. *Academic Radiology 11*(9), 1011–1021.

Atilla P. Kiraly, Eric Pichon, D. P. N. and C. L. Novak (2004). Analysis of arterial sub-trees affected by pulmonary emboli. In *Proceedings of SPIE (Medical Imaging)*, Volume 5370, pp. 1720–1729. The International Society for Optical Engineering.

Binsheng Zhao, Gordon Gamsu, M. S. G. L. J. and L. H. Schwartz (2003). Automatic detection of small lung nodules on ct utilizing a local density maximum algorithm. *Journal of Applied Clinical Medical Physics 4*(3), 248–260.

Chen, S. and R. M. Haralick (1995). Recursive erosion, dilation, opening, and closing transforms. *IEEE Transactions on Image Processing 4*(3), 335–345.

Cornelis M. van Bemmel, Luuk J. Spreeuwers, M. A. V. and W. J. Niessen (2003). Level-set-based arter-vein separation in blood pool agent ce-mr angiograms. *IEEE Transactions on Medical Imaging 22*(10), 1224–1234.

Gady Agam, Samuel G. Armato, I. . C. W. (2005). Vessel tree reconstruction in thoracic ct scans with application to nodule detection. *IEEE Transaction on Medical Imaging 24*(4), 486–499.

Hartmann, I. and M. Prokop (2002). Spiral ct in the diagnosis of acute pulmonary embolism. *Medica Mundi 46*(3), 2–11.

Ingmar Bitter, A. E. K. and M. Sato (2001). Penalized-distance volumetric skeleton algorithm. *IEEE Transactions on Visualization and Computer Graphics 7*(3), 195–206.

Ingrid Sluimer, Arnold Schilham, M. P. and B. van Ginneken (2006). Comptuer analysis of computed tomography scans of the lung: Survey. *IEEE Transactions on Medical Imaging 25*(4), 385–405.

Jamshid Dehmeshki, Xujiong Ye, F. W. X. Y. L. M. A. M. S. and S. Qanadli (2004, September). An accurate and reproducible scheme for quantification of coronary artery calcification in ct scans. In *Proceedings of the 26th Annual International Conference of IEEE EMBS*, pp. 1918–1921. IEEE: The International Society for Optical Engineering.

Katja Bühler, P. F. and A. L. Cruz (2003). Geometric methods for vessel visualization and quantification- a survey. In H. M. G. Brunnett, B. Hamann (Ed.), *Geometric Modelling for Scientific Visualization*, pp. 1–24. Springer.

Kirbas, C. and F. Quek (2004). A review of vessel extraction techniques and algorithms. *ACM Computing Surveys (CSUR) 36*(2), 81–121.

Michael Bock, Stefan O. Schoenberg, F. F. a. L. R. S. (2000). Separation of arteries and veins in 3d mr angiography using correlation analysis. *IEEE Transactions on Medical Imaging 43*, 481–487.

Saito, T. and J.-I. Toriwaki (1994). New algorithms for euclidean distance transformation of an *n*-dimensinal digitized picture with applications. *Pattern Recognition 27*(11), 1551–1565.

Schoepf, U. J. and P. Costello (2004). Ct angiography for diagnosis of pulmonary embolism: State of the art. *Radiology 230*(2), 329–337.

Shiying Hu, E. A. H. and J. M. Reinhardt (2001). Automatic lung segmentation for accurate quantitation of volumetric x-ray ct images. *IEEE Transactions on Medical Imaging 20*(6), 490–498.

Stefancik, R. M. and M. Sonka (2001). Highly automated segmentation of arterial and venous trees from three-dimensional magnetic resonance angiography (mra). *The International Journal of Cardiovascular Imaging 17*, 37–47.

Tianhu Lei, Jayaram K. Udupa, P. K. S. and D. Odhner (2001). Artery-vein separation via mra - an image processing approach. *IEEE Transactions on Medical Imaging 20*(8), 689–703.

Tomas Bülow, Fafael Wiemker, T. B. C. L. . S. R. (2005). Automatic extraction of the pulmonary artery tree from multi-slice ct data. *Medical Imaging 2005: Physiology, Function, and Structure from Medical Images 6*(23), 730–740.

Yoshitaka Masutani, H. M. . J. D. (2002). Computerized detection of pulmonary embolism in spiral ct angiography based on volumetric image analysis. *IEEE Transaction on Medical Imaging 21*(12), 1517–1523.